Synergistic Stabilization of $CsPbI_3$ Inorganic Perovskite via 1D Capping and Secondary Growth

Jingya Mi[a,b], Yuetian Chen[b*], Xiaomin Liu[b], Xingtao Wang[b], Yanfeng Miao[b], Yabing Qi[c], and Yixin Zhao[b*]

[a] *China-UK Low Carbon College, Shanghai Jiao Tong University, Shanghai 201306, China.*
[b] *School of Environmental Science and Engineering, Frontiers Science Center for Transformative Molecules, Shanghai Jiao Tong University, Shanghai 200240, China.*
[c] *Energy Materials and Surface Sciences Unit (EMSSU), Okinawa Institutes of Science and Technology Graduate University (OIST), Okinawa 904-0495, Japan.*

[*]Corresponding author.

E-mail address: yixin.zhao@sjtu.edu.cn, yuetian.chen@sjtu.edu.cn

Abstract

Cesium lead iodide ($CsPbI_3$) perovskite has gained great attention in the photovoltaic (PV) community because of its unique optoelectronic properties, good chemical stability and appropriate bandgap for sunlight harvesting applications. However, compared to solar cells fabricated from organic-inorganic hybrid perovskites, the commercialization of devices based on all-inorganic $CsPbI_3$ perovskites still faces many challenges regarding PV performance and long-term stability. In this work, we discovered that tetrabutylammonium bromide (TBABr) post-treatment to $CsPbI_3$ perovskite films could achieve synergistic stabilization with both TBA^+ cation intercalation and Br-doping. Such TBA^+ cation intercalation leads to one-dimensional capping with $TBAPbI_3$ perovskite formed *in situ*, while the Br-induced crystal secondary growth helps effectively passivate the defects of $CsPbI_3$ perovskite, thus enhancing the stability. In addition, the incorporation of TBABr can improve energy-level alignment and reduce interfacial charge recombination loss for better device performance. Finally, the highly stable TBABr-treated $CsPbI_3$-based perovskite solar cells show reproducible photovoltaic performance with a champion efficiency up to 19.04%, while retaining 90% of the initial efficiency after 500 h storage without

encapsulation.

Keywords: $CsPbI_3$ inorganic perovskite; All-inorganic perovskite solar cell; One-dimensional capping; Synergistic stabilization

1. Introduction

Perovskite solar cell (PSC) exhibits great intrinsic properties as a promising candidate for the next-generation photovoltaic technologies [1-4]. With significant technical and theoretical accomplishments made in many aspects over the past decade, the highest certified power conversion efficiency (PCE) of PSC has reached 25.5%, which is close to that of the commercialized monocrystalline silicon solar cells [5-7]. Though organic-inorganic hybrid metal halide perovskites have achieved significant progress owing to their unique properties and compositional versatility [8-10], they still face a great challenge of long-term stability owing to the decomposition of labile organic cation components, i.e., methylammonium (MA^+) or formamidinium (FA^+), from crystal lattice, which is believed to be the reason for their relatively poor thermal and chemical stability. In particular, $MAPbI_3$ degrades easily at low temperature that can be attribute to the high volatility and rotational freedom of MA^+ [11, 12]. Therefore, long-term stability of these organic-inorganic hybrid perovskite materials has become the main limiting factor for their commercial applications [13, 14].

Alternatively, all-inorganic $CsPbI_3$ perovskites possess suitable bandgap (≈1.7 eV) with no volatile organic component in the crystal lattice [15-19]. Their employment for photovoltaics has achieved considerable progress [20]. They have demonstrated PCEs exceeding 20% and high chemical stabilities, making the composition one of the most promising for fabricating chemically stable and high-efficiency PSCs [21-25].

However, black phase $CsPbI_3$ perovskites tend to convert into non-perovskite yellow phase at room temperature [26, 27]. Various strategies including interface engineering, dimensional engineering, organic cation surface termination, and elemental alloying have been developed to improve their performance and stability [20, 28-34]. For example, Br induced crystal secondary growth is an effective strategy for perovskite passivation [25, 35, 36]. Post-treatment with organic cation halide salts such as

phenethylammonium iodide (PEAI) to form a low-dimensional capping layer has also been demonstrated to be effectual in passivating defects for organic-inorganic hybrid perovskites [22, 37-39]. However, previous studies have also suggested that for inorganic perovskites, such post-treatment would not easily induce the formation of low-dimensional perovskite [31, 32]. This is due to the strong binding strength of cesium ions in inorganic perovskite, which could not be easily extracted from the lattice. Therefore, for stabilizing and passivating inorganic perovskite, the conventional route of post-treatment to form low dimensional perovskite *in situ* is demanding. Very recently, our group reported for the first time that tetrabutylammonium (TBA^+) cation can intercalate into $CsPbI_3$ to substitute Cs^+ cation and to form an one-dimensional (1D) $TBAPbI_3$ perovskite layer, which improved the PSC device's stability and PCE [40].

Herein, we report an effective synergistic stabilization strategy using tetrabutylammonium bromide (TBABr). Our findings show that the concurrent introduction of TBA^+ cation and Br^- anion could achieve a bifunctional stabilization including both TBA^+ cation intercalation and Br doping. The Br-induced crystal secondary growth and the *in situ* formation of 1D $TBAPbI_3$ capping layer help effectively passivate the defects of $CsPbI_3$ perovskite. The synergistic passivation and stabilization could reduce the trap density and prolong the charge carrier lifetime, resulting in enhanced device performance and stability. The fabricated TBABr-$CsPbI_3$-based PSCs exhibited a champion efficiency up to 19.04% with decent stability against various environmental factors.

2. Experimental

2.1 Materials

Lead iodide (PbI_2, 99.999%), cesium iodide (CsI, 99.999%) and dimethylamine solution (DMA, 40 wt% aqueous solution) were purchased from Alfa Aesar. Tetrabutylammonium bromide (TBABr, 99.0%) was purchased from Macklin. Hydroiodic acid (HI, 57 wt% aqueous solution) was purchased from Sigma-Aldrich. N, N- Dimethylformamide (DMF), isopropanol (IPA), chlorobenzene (CB), diethyl ether, and ethyl alcohol were purchased from J&K Scientific Ltd.

Dimethylammonium iodide (DMAI) used for black phase $CsPbI_3$ film formation was synthesized by following steps: dimethylamine solution and hydroiodic acid (molar ratio: 1:1.5) were mixed and stirred for 4 h under ice-bath condition; then the mixture was dried by rotary evaporation, washed with ethyl alcohol and diethyl ether; precipitates were recovered and dried in vacuum for 24 h to obtain the target product.

2.2 Device fabrication

Compact TiO_2 layer was deposited on patterned FTO (TEC-7) substrate by spray pyrolysis with 0.2 M titanium bis(ethyl acetoacetate)-diisopropoxide 1-butanol solution at 450 °C and annealed at 450 °C for 1 hour. A 0.7 M precursor solution was made by dissolving CsI, PbI_2 and DMAI (molar ratio: 1:1:1.2) in anhydrous DMF. Then the precursor solution was deposited using a one-step spin-coating process at 3000 rpm for 30 s onto a prewarmed FTO/TiO_2 substrate, and then annealed at 210 °C for 5 min. For surface treatment, 100 μL TBABr-IPA solution (1, 2, 4 mg/mL) was spin-coated at 3000 rpm for 30s onto the perovskite film and the film was annealed at 100 °C for 3 min. 0.1 M spiro-OMeTAD, 0.035 M bis(trifluoromethane) sulfonamide lithium salt (Li-TFSi) and 0.12 M 4-tert-butylpyridine (tBP) were dissolved in chlorobenzene/acetonitrile (10:1, v/v) as the solution for hole transport layer deposition. The mixed solution was then spin-coated at 4000 rpm for 25 s onto the perovskite film. Finally, Ag layer of ~100 nm thick was thermally evaporated under vacuum and deposited as top electrode.

2.3 Characterization

X-ray diffraction (XRD) patterns were collected on a Shimadzu XRD-6100 diffractometer equipped with Cu Kα radiation. Ultraviolet photoelectron spectroscopy (UPS) and X-ray photoelectron spectroscopy (XPS) were conducted on an X-ray photoelectron spectrometer (Kratos AXIS Ultra DLD) with different light sources (He Iα = 21.2 eV for UPS and monochromated Al Kα = 1486.6 eV for XPS). UV-vis absorption spectra were measured by Cary-60 UV-vis spectrophotometer. Surface morphologies of the perovskite thin films were characterized by scanning electron microscope (SEM, JEOL JSM-7800F Prime), and atomic force microscope (AFM,

Bruker Dimension FastScan Bio) on tapping mode. Synchrotron-based grazing-incidence wide-angle X-ray scattering (GIWAXS) was carried out at BL14B1 line station of Shanghai Synchrotron Radiation Facility with beam wavelength of 0.12398 nm. Steady-state and time-resolved photoluminescence (PL) spectra were obtained on FLS1000 Photoluminescence Spectrometer (Edinburgh Instruments Ltd.) using a 445 nm excitation laser. Transient photocurrent (TPC) and transient photovoltage (TPV) spectra were measured by a microsecond pulse of white light incident on the devices under short-circuit condition and open-circuit condition, respectively. *J-V* curves were recorded on a digital source meter (Keithley 2401) under AM 1.5G simulated sunlight (100 $mW \cdot cm^{-2}$). The scan rate is set to 0.05 V / s for the measurement. External quantum efficiency (EQE) was measured on Enlitech QE-3011 system. All the TPC/TPV, *J-V*, EQE measurements were conducted in atmosphere.

3. Results and discussion

In this work, a specific quaternary ammonium halide, TBABr, was designed to purposefully passivate the defects in the inorganic $CsPbI_3$ perovskite thin film. The $CsPbI_3$ films were treated by spin-coating different concentrations (1, 2, 4 mg/mL) of TBABr-IPA solution. Among the trial experiments, $CsPbI_3$ treated with 2 mg/mL TBABr was found to be the optimal concentration for enhancement on stability and PV performance. Therefore, hereinafter, the notation of TBABr-$CsPbI_3$ refers to the samples treated with this specific concentration.

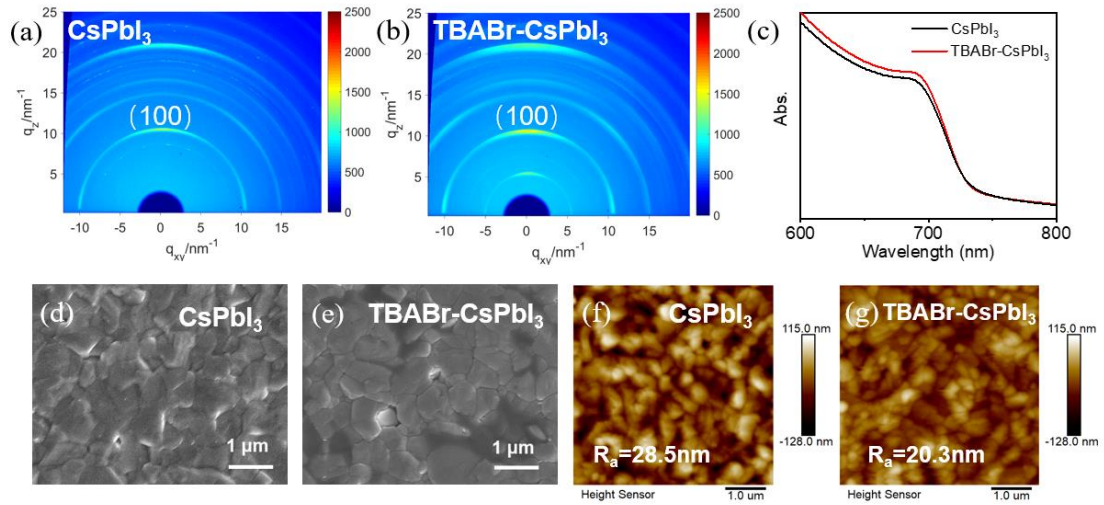

Fig. 1. GIWAXS data of (a) $CsPbI_3$ and (b) TBABr-$CsPbI_3$ thin films; (c) UV-Vis spectra of $CsPbI_3$ and TBABr-$CsPbI_3$ thin films; SEM images of (d) $CsPbI_3$ and (e) TBABr-$CsPbI_3$ thin films; AFM images of (f) $CsPbI_3$ and (g) TBABr-$CsPbI_3$ thin films.

GIWAXS analysis was performed to investigate the crystalline features of the resulting films. In general, the perovskite films have good crystallinity and grow preferably along the (100) direction of $CsPbI_3$. TBABr-$CsPbI_3$ films showed stronger diffraction strength with obvious (100) orientation (**Fig. 1a-b, S2**). Additionally, compared to the reference one, the stronger diffraction spot at q_z=10 nm^{-1} indicated the formation of a vertically oriented crystalline TBABr-$CsPbI_3$ film. Moreover, a new diffraction ring at q_z=5.2 nm^{-1} was observed, which appeared to be more obvious as the concentration of TBABr increased (Fig. S2). Since the peak position was consistent with the previously reported 1D $TBAPbI_3$ layer and this characteristic peak can be ascribed to its (200) plane [40], the occurrence of this peak is the signal of the formation of low dimensional perovskite $TBAPbI_3$, suggesting that TBABr can intercalate into $CsPbI_3$ to form a low dimensional structure. XRD results of the perovskite films treated with different concentrations of TBABr are shown in **Fig. S1**. With the increase of TBABr concentration, the magnified (110) and (220) peaks shift to higher angles, which is probably because of the incorporation of the smaller Br^- ion into the lattice.

The UV-vis spectra of the pristine $CsPbI_3$ and TBABr-$CsPbI_3$ films (**Fig. 1c**) showed that the TBABr treatment has a slight effect on the absorption profiles. With the increase

of TBABr concentration (**Fig. S3**), the absorption edges of corresponding films slightly deviated from the previous one with lower degree of treatment. The broadened bandgap with respect to the previously reported black phase β-$CsPbI_3$ perovskite [20] indicates the successful incorporation of Br.

The morphology of TBABr-$CsPbI_3$ films exhibited a legible improvement. Top-view SEM images (**Fig.1d-e** and **S4**) show that the surface morphology of TBABr-$CsPbI_3$ film becomes more compact and smoother compared to the control, which may be related to crystal secondary growth. In addition, some small pinholes have been effectively eliminated. AFM height images showed that the roughness of the TBABr-$CsPbI_3$ film surface (R_a = 20.3 nm) was lower than that of the control (R_a = 28.5 nm) (**Fig. 1f-g, S5**). These characterization results confirm that the perovskite film morphology exhibits an improvement via TBABr treatment. Such a beneficial effect may be originated from Br-induced crystal secondary growth and the formation of 1D $TBAPbI_3$ perovskite layer.

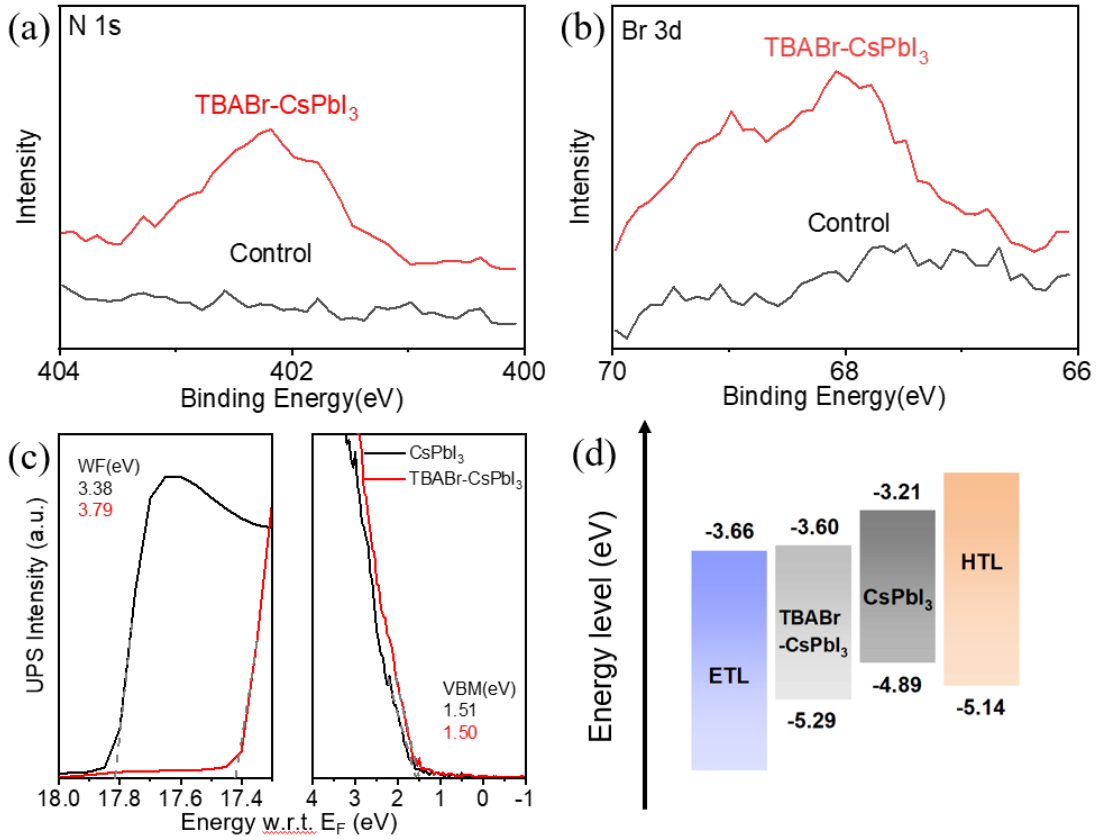

Fig. 2. High resolution XPS (a) N *1s* and (b) Br *3d* core-level spectra for $CsPbI_3$ control

and TBABr-$CsPbI_3$; (c) UPS spectra of the $CsPbI_3$ and TBABr-$CsPbI_3$ thin films that correspond to the secondary electron onset and valence band regions; (d) Energy level diagram for the solar cell architecture.

XPS measurements were performed to investigate the chemical composition of the TBABr-$CsPbI_3$ and $CsPbI_3$ films (**Fig. 2a-b, S6**). Peaks of N *1s* and Br *3d* were detected with TBABr treatment. The occurrence of N *1s* confirmed the existence of the TBA^+ cation, and the small amount of $CsPbI_3$ converted into 1D $TBAPbI_3$ perovskite. Meanwhile, the peak of Br *3d* identified that the crystal structure was doped with bromine.

UPS was used to measure energy band position of the $CsPbI_3$ and TBABr-$CsPbI_3$ films. The work function (WF) is defined as the difference between the binding energy of the secondary electron cutoff and the incident photon energy (21.2 eV). TBABr-$CsPbI_3$ showed a higher WF by about 0.41 eV and the valance band region of 1.50 eV (**Fig. 2c**). Based on these results (detailed data in Table S1), the band alignment between the perovskite layer and the charge transport layers in a PSC architecture is presented in **Fig. 2d** where TiO_2 is used for ETL and spiro-OMeTAD for HTL. Compared to pristine $CsPbI_3$ film, the energy band of the TBABr-$CsPbI_3$ film shifted to more negative position. The values of conduction band minimum (CBM) of $CsPbI_3$ and TBABr-$CsPbI_3$ perovskite films are calculated as −3.60 eV and −3.21 eV, respectively. This shift decreased the energy difference between the CBM of TiO_2 and the perovskite layer, which could expedite the electron transport from the perovskite to the TiO_2 layer in devices. The adjusted alignment between the valence band maximum (VBM) of TBABr-$CsPbI_3$ could also facilitate the hole extraction from the perovskite to the spiro-OMeTAD hole transport layer. Therefore, the post-treatment with TBABr improved energy-level alignment at both the perovskite/ETL and the perovskite/HTL interfaces, which can help reduce interfacial charge recombination loss, and furthermore promoting PV performance.

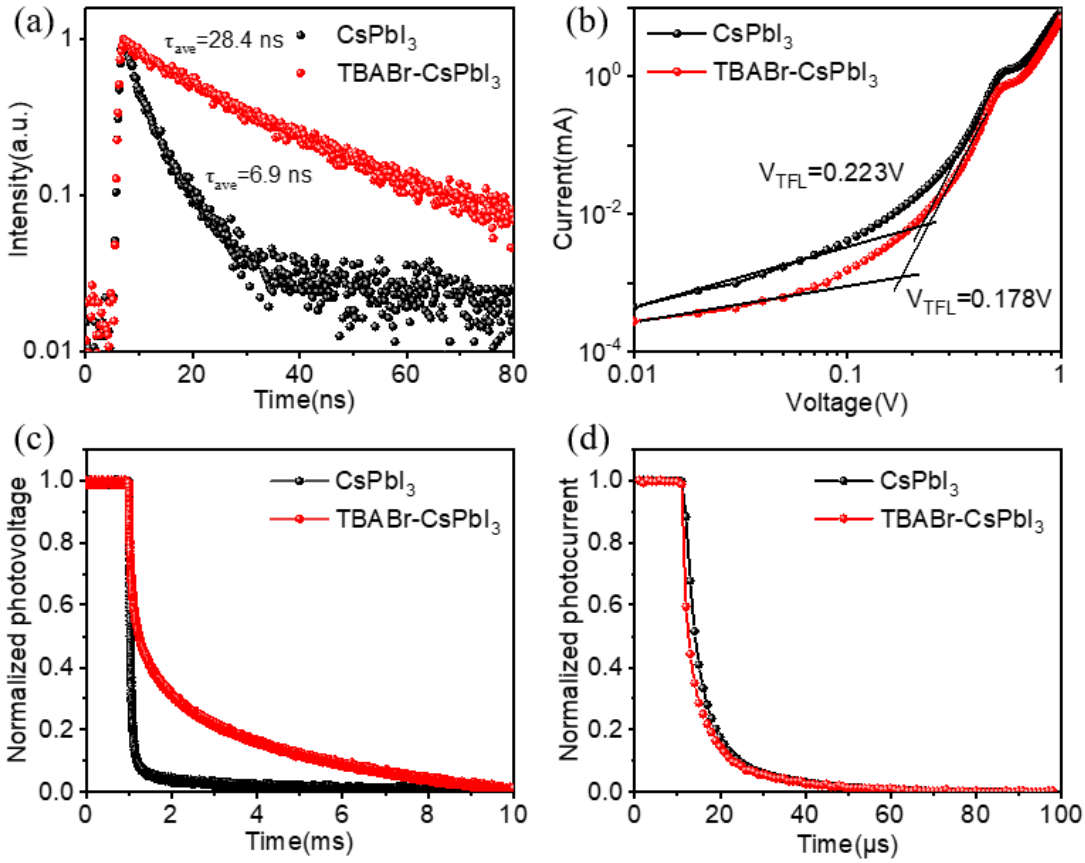

Fig. 3. (a) TRPL spectra of the $CsPbI_3$ and TBABr-$CsPbI_3$ thin films; (b) Dark *J-V* curves of the electron-only devices based on $CsPbI_3$ and TBABr-$CsPbI_3$; (c) TPV and (d) TPC curves of the $CsPbI_3$ and TBABr-$CsPbI_3$ based devices.

Steady-state PL and TRPL measurements are performed on $CsPbI_3$ and TBABr-$CsPbI_3$ films to evaluate the effect of TBABr treatment on excitonic quality. The PL intensity of TBABr-$CsPbI_3$ film was about 4 times higher compared with that of control (**Fig. S7**), indicating that the TBABr-$CsPbI_3$ films have a lower defect density and the non-radiative recombination has been significantly suppressed [41]. The TRPL spectra (**Fig. 3a**) were fitted with the following biexponential decay function: $Y = A_1 e^{-\frac{x}{\tau_1}} + A_2 e^{-\frac{x}{\tau_2}}$. τ_1 and τ_2 are the fast and slow decay time constants. A_1 and A_2 are the coefficients that represent the contribution of each time constant to the normalized biexponential decay. The average charge-carrier lifetime of TBABr-$CsPbI_3$ film (τ_{ave}=28.4 ns) was calculated to be about 4 times higher than the control one (τ_{ave}=6.9

ns), revealing the significant increase of charge carrier lifetime. The prolonged carrier lifetime was consistent with the suppressed non-radiative recombination from the steady-state PL results, suggesting effective defect passivation by the dual functionalization with TBABr treatment.

Trap density (N_t) was quantified using the space-charge-limited current (SCLC) test on electron-only devices with the structure of FTO/TiO_2/perovskite/[6,6]-phenyl-C61-butyric acid methyl ester (PCBM)/Ag. The corresponding dark current-voltage (*J-V*) curves are shown in **Fig. 3b**, in which the trap-filled limit voltages (V_{TFL}) of TBABr-$CsPbI_3$ and $CsPbI_3$ perovskite were measured to be 0.178V and 0.223V, respectively. Since the value of V_{TFL} is determined by the trap state, N_t can be calculated from the following equation:

$$V_{TFL} = \frac{eN_tL^2}{2\varepsilon_r\varepsilon_0}$$

where e represents the elementary charge, ε_r is the relative dielectric constant and equals to 6.32 for $CsPbI_3$, ε_0 is the vacuum permittivity, L is the thickness of the perovskite layer [42]. Thus, N_t values are calculated to be 7.7×10^{14} cm^{-3} and 9.9×10^{14} cm^{-3} for TBABr-$CsPbI_3$ and $CsPbI_3$ perovskite devices, respectively. The trap density is thus reduced by TBABr treatment, which indicates effective passivation of trap states.

In addition, we further investigated the charge-transport properties of the $CsPbI_3$ and TBABr-$CsPbI_3$ based PSCs by TPC and TPV measurements. TPV curve of the TBABr-$CsPbI_3$ based PSC in **Fig. 3c** showed a longer charge-carrier lifetime than that of the reference device, indicating a significant decrease of undesired charge-carrier recombination. Meanwhile, as shown in **Fig. 3d**, the TBABr-$CsPbI_3$ based PSC device exhibit a faster TPC response than that of the reference device, suggesting better charge transport or collection efficiency. The above results showed that TBABr treatment can effectively passivate the defects in perovskite films. Since the density of defects in perovskite films can directly influence the device performance, we expect that TBABr treatment can facilitate the fabrication of high-efficiency PSCs with good stability.

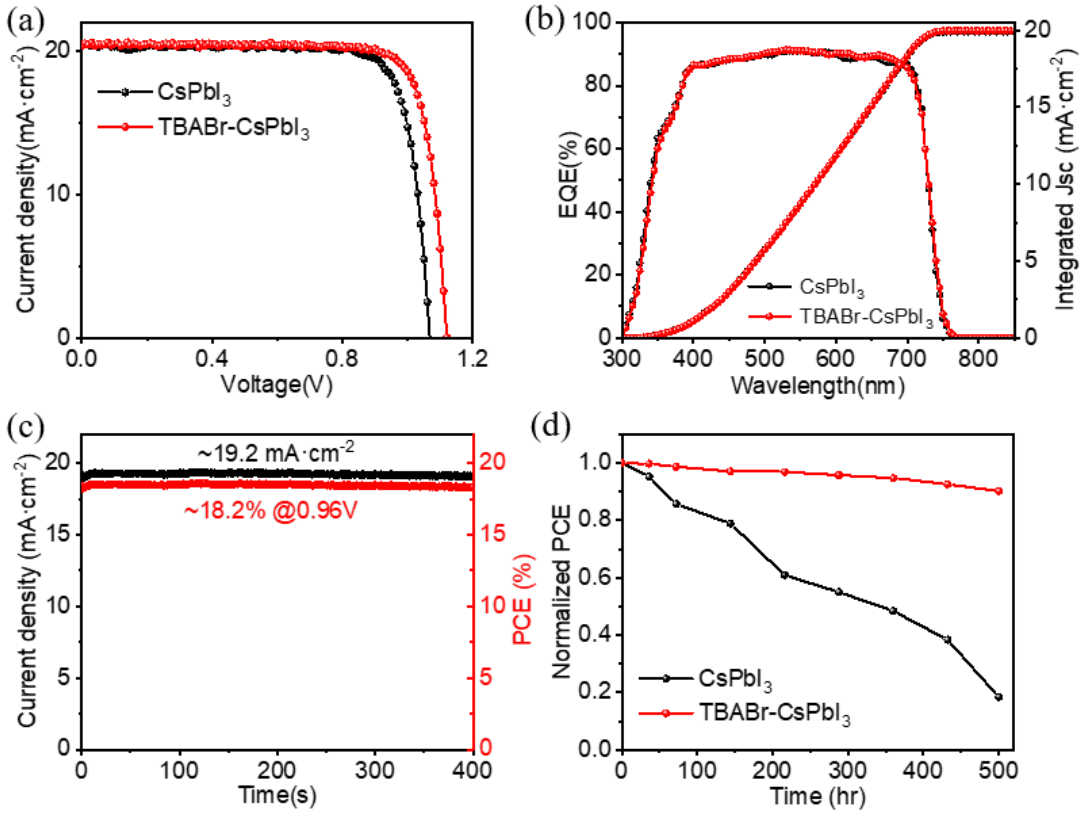

Fig. 4. (a) *J-V* curves of the $CsPbI_3$ and TBABr-$CsPbI_3$ based PSCs; (b) EQE spectra and integrated J_{SC} curves for the $CsPbI_3$ and TBABr-$CsPbI_3$ based PSCs; (c) Stable output curve of the champion TBABr-$CsPbI_3$ based PSC; (d) Storage stability of the unencapsulated $CsPbI_3$ and TBABr-$CsPbI_3$ based PSCs in ambient air with humidity of 30-40%.

To evaluate the influence of TBABr treatment on the PV performance of PSCs, we fabricated PSCs of the $CsPbI_3$ layer with and without TBABr treatment employing the device architecture of FTO/TiO_2/perovskite/spiro-OMeTAD/Ag. The TBABr treated devices exhibit better reproducibility and higher photovoltaic performance than that of the control device (**Fig. S8**). The PCE enhancement was mainly attributed to the significant improvements on open circuit voltage (V_{OC}) and fill factor (FF), which can be ascribed to the synergistic effect of defect passivation and better energy-level alignment. The TBABr-$CsPbI_3$ based PSCs exhibit a champion efficiency of 19.04%, with a V_{OC} of 1.121V, short-circuit current density (J_{SC}) of 20.64 mA cm^{-2} and FF of 82.3% (**Fig. 4a**). External quantum efficiency (EQE) and integrated J_{SC} curves of the

cells are presented in **Fig. 4b**. The integration of EQE curve leads to J_{SC} of 20.01 mA/cm^2, which is only ~3.20% lower than the *J-V* result. As shown in **Fig. 4c**, a champion TBABr-$CsPbI_3$ based device exhibits a good stable output performance. The cell gives a current density output of 19.2 mA/cm^2 and a stabilized PCE of over 18.2% at the maximum power point of 0.96 V.

The overall stability improvement introduced by TBABr treatment is also quite evident. TBABr-$CsPbI_3$ thin film showed better thermal stability than that of the control (**Fig. S9a**). The phase pure β-$CsPbI_3$ turned into the yellow δ phase after 75 °C annealing for 7 days, while the TBABr-$CsPbI_3$ thin film showed no occurrence of any impurity phase peaks under the same condition, suggesting enhanced thermal stability. Considering that moisture resistance was another significant challenge for all-inorganic perovskite, further humidity test in 80 ± 5% relative humidity (RH) at 25 °C showed that the TBABr-$CsPbI_3$ thin film has better stability than that of the control (**Fig. S9b)**. The black $CsPbI_3$ film turned yellow within 0.5 h, while TBABr-$CsPbI_3$ thin film retained the pure black phase under the same condition.

For the fabricated devices, along with the enhanced PV performance, TBABr-$CsPbI_3$-based PSCs also exhibit better stability than $CsPbI_3$-based PSCs. We evaluated the storage stability of PSCs with and without TBABr treatment. As shown in **Fig. 4d**, unencapsulated devices were stored in ambient conditions (25 °C, 30-40% RH) for 500 h. The TBABr-$CsPbI_3$-based PSC maintained ~90% of its initial PCE, while the PCE of $CsPbI_3$-based PSC rapidly dropped to ~20% of its initial value under the same condition. The stability enhancement reflected on both thin films and devices proved the effectiveness of the synergistic stabilization on $CsPbI_3$ via the 1D capping and secondary growth by TBABr incorporation.

4. Conclusions

In summary, we introduced a bifunctional stabilization strategy including both Br incorporation and *in situ* formation of low-dimensional perovskite for efficient and stable $CsPbI_3$-based solar cells. Synergistic stabilization of the perovskite structure was achieved with both TBA^+-induced one-dimensional capping and Br-induced crystal

secondary growth. This strategy effectively passivated defects and improved energy-level alignment, which can help reduce nonradiative and interfacial charge recombination loss. Thus, the TBABr-$CsPbI_3$ thin films showed better phase stability and the fabricated PSCs exhibited remarkably improved V_{OC} and FF, achieving a champion PCE of 19.04%. The corresponding unencapsulated device also exhibited better stability. In general, this dual-functional strategy can effectively enhance both PV performance and stability of PSCs. This work provides promising directions of developing bifunctional strategies of both halide doping and 1D *in situ* perovskite formation to synergistically stabilize all-inorganic perovskites for optoelectronic applications.

Acknowledgments

Y. Z. acknowledges the support from the National Natural Science Foundation of China (Grant Numbers 22025505, 51861145101, 21777096), Program of Shanghai Academic/Technology Research Leader (Grant Number 20XD1422200), and the Key Laboratory of Resource Chemistry, Ministry of Education (KLRC_ME2003). Y. B. Q. acknowledges the support from the Energy Materials and Surface Sciences Unit of the Okinawa Institute of Science and Technology Graduate University.

References:

1. A. Kojima, K. Teshima, Y. Shirai, and T. Miyasaka, J. Am. Chem. Soc. **131** (2009) 6050-6051.
2. M. Liu, M.B. Johnston, and H.J. Snaith, Nature. **501** (2013) 395-398.
3. N.-G. Park, M. Grätzel, T. Miyasaka, K. Zhu, and K. Emery, Nat. Energy. **1** (2016) 16152.
4. A.K. Jena, A. Kulkarni, and T. Miyasaka, Chem. Rev. **119** (2019) 3036-3103.
5. J.Y. Kim, J.W. Lee, H.S. Jung, H. Shin, and N.G. Park, Chem. Rev. **120** (2020) 7867-7918.
6. H. Min, D.Y. Lee, J. Kim, G. Kim, K.S. Lee, J. Kim, M.J. Paik, Y.K. Kim, K.S. Kim, M.G. Kim, T.J. Shin, and S. Il Seok, Nature. **598** (2021) 444-450.
7. National Renewable Energy Laboratory, Best research-cell efficiencies chart (2021); https://www.nrel.gov/pv/cell-efficiency.html.
8. N.J. Jeon, J.H. Noh, W.S. Yang, Y.C. Kim, S. Ryu, J. Seo, and S.I. Seok, Nature. **517** (2015) 476-480.
9. Y. Zhao and K. Zhu, Chem. Soc. Rev. **45** (2016) 655-689.
10. P.D. Matthews, D.J. Lewis, and P. O'Brien, J. Mater. Chem. A. **5** (2017) 17135-17150.
11. S. Wang, Y. Jiang, Emilio J. Juarez-Perez, Luis K. Ono, and Y. Qi, Nat. Energy. **2** (2016) 16195.
12. S.-H. Turren-Cruz, A. Hagfeldt, and M. Saliba, Science. **362** (2018) 449-453.
13. C.C. Boyd, R. Cheacharoen, T. Leijtens, and M.D. McGehee, Chem. Rev. **119** (2019) 3418-3451.
14. M. Hu, M. Chen, P. Guo, H. Zhou, J. Deng, Y. Yao, Y. Jiang, J. Gong, Z. Dai, Y. Zhou, F. Qian, X. Chong, J. Feng, R.D. Schaller, K. Zhu, N.P. Padture, and Y. Zhou, Nat. Commun. **11** (2020) 151.
15. G.E. Eperon, G.M. Paternò, R.J. Sutton, A. Zampetti, A.A. Haghighirad, F. Cacialli, and H.J. Snaith, J. Mater. Chem. A. **3** (2015) 19688-19695.
16. J. Liang, C. Wang, Y. Wang, Z. Xu, Z. Lu, Y. Ma, H. Zhu, Y. Hu, C. Xiao, X. Yi, G. Zhu, H. Lv, L. Ma, T. Chen, Z. Tie, Z. Jin, and J. Liu, J. Am. Chem. Soc. **138** (2016) 15829-15832.
17. A. Ho-Baillie, M. Zhang, C.F.J. Lau, F.-J. Ma, and S. Huang, Joule. **3** (2019) 938-955.
18. Y. Zhou and Y. Zhao, Energy Environ. Sci. **12** (2019) 1495-1511.
19. Y. Wang, Y. Chen, T. Zhang, X. Wang, and Y. Zhao, Adv. Mater. **32** (2020) e2001025.
20. Y. Wang, M.I. Dar, L.K. Ono, T. Zhang, M. Kan, Y. Li, L. Zhang, X. Wang, Y. Yang, X. Gao, Y. Qi, M. Grätzel, and Y. Zhao, Science. **365** (2019) 591.
21. F. Bai, J. Zhang, Y. Yuan, H. Liu, X. Li, C.C. Chueh, H. Yan, Z. Zhu, and A.K. Jen, Adv. Mater. **31** (2019) e1904735.
22. P. Chen, Y. Bai, S. Wang, M. Lyu, J.H. Yun, and L. Wang, Adv. Funct. Mater. **28** (2018) 1706923.
23. W. Chen, X. Li, Y. Li, and Y. Li, Energy Environ. Sci. **13** (2020) 1971-1996.
24. B. Yu, J. Shi, S. Tan, Y. Cui, W. Zhao, H. Wu, Y. Luo, D. Li, and Q. Meng, Angew. Chem. Int. Ed. **60** (2021) 13436-13443.
25. X. Wang, Y. Wang, Y. Chen, X. Liu, and Y. Zhao, Adv. Mater. **33** (2021) 2103688.
26. A. Marronnier, G. Roma, S. Boyer-Richard, L. Pedesseau, J.M. Jancu, Y. Bonnassieux, C. Katan, C.C. Stoumpos, M.G. Kanatzidis, and J. Even, ACS Nano. **12** (2018) 3477-3486.
27. J.A. Steele, H. Jin, I. Dovgaliuk, R.F. Berger, T. Braeckevelt, H. Yuan, C. Martin, E. Solano, K. Lejaeghere, S.M.J. Rogge, C. Notebaert, W. Vandezande, K.P.F. Janssen, B. Goderis, E.

Debroye, Y.-K. Wang, Y. Dong, D. Ma, M. Saidaminov, H. Tan, Z. Lu, V. Dyadkin, D. Chernyshov, V.V. Speybroeck, E.H. Sargent, J. Hofkens, and M.B.J. Roeffaers, Science. **365** (2019) 679-684.

28. J. Zhang, Z. Jin, L. Liang, H. Wang, D. Bai, H. Bian, K. Wang, Q. Wang, N. Yuan, J. Ding, and S.F. Liu, Adv. Sci. **5** (2018) 1801123.
29. T. Zhang, M.I. Dar, G. Li, F. Xu, N. Guo, M. Grätzel, and Y. Zhao, Sci. Adv. **3** (2017) e1700841.
30. Y. Jiang, J. Yuan, Y. Ni, J. Yang, Y. Wang, T. Jiu, M. Yuan, and J. Chen, Joule. **2** (2018) 1356-1368.
31. Y. Wang, T. Zhang, M. Kan, Y. Li, T. Wang, and Y. Zhao, Joule. **2** (2018) 2065-2075.
32. Y. Wang, T. Zhang, M. Kan, and Y. Zhao, J. Am. Chem. Soc. **140** (2018) 12345-12348.
33. F. Liu, C. Ding, Y. Zhang, T.S. Ripolles, T. Kamisaka, T. Toyoda, S. Hayase, T. Minemoto, K. Yoshino, S. Dai, M. Yanagida, H. Noguchi, and Q. Shen, J. Am. Chem. Soc. **139** (2017) 16708-16719.
34. Q. Ye, Y. Zhao, S. Mu, F. Ma, F. Gao, Z. Chu, Z. Yin, P. Gao, X. Zhang, and J. You, Adv. Mater. **31** (2019) e1905143.
35. M. Yang, T. Zhang, P. Schulz, Z. Li, G. Li, D.H. Kim, N. Guo, J.J. Berry, K. Zhu, and Y. Zhao, Nat. Commun. **7** (2016) 12305.
36. D. Luo, W. Yang, Z. Wang, A. Sadhanala, Q. Hu, R. Su, R. Shivanna, G.F. Trindade, J.F. Watts, Z. Xu, T. Liu, K. Chen, F. Ye, P. Wu, L. Zhao, J. Wu, Y. Tu, Y. Zhang, X. Yang, W. Zhang, R.H. Friend, Q. Gong, H.J. Snaith, and R. Zhu, Science. **360** (2018) 1442-1446.
37. Y. Lin, Y. Bai, Y. Fang, Z. Chen, S. Yang, X. Zheng, S. Tang, Y. Liu, J. Zhao, and J. Huang, J. Phys. Chem. Lett. **9** (2018) 654-658.
38. S. Yang, Y. Wang, P. Liu, Y.-B. Cheng, H.J. Zhao, and H.G. Yang, Nat. Energy. **1** (2016) 15016.
39. Z. Yuan, C. Zhou, Y. Tian, Y. Shu, J. Messier, J.C. Wang, L.J. van de Burgt, K. Kountouriotis, Y. Xin, E. Holt, K. Schanze, R. Clark, T. Siegrist, and B. Ma, Nat Commun. **8** (2017) 14051.
40. X. Liu, X. Wang, T. Zhang, Y. Miao, Z. Qin, Y. Chen, and Y. Zhao, Angew. Chem. Int. Ed. **60** (2021) 12351-12355.
41. X. Zheng, B. Chen, J. Dai, Y. Fang, Y. Bai, Y. Lin, H. Wei, Xiao C. Zeng, and J. Huang, Nat. Energy. **2** (2017) 17102.
42. J. Kim, B. Koo, W.H. Kim, J. Choi, C. Choi, S.J. Lim, J.-S. Lee, D.-H. Kim, M.J. Ko, and Y. Kim, Nano Energy. **66** (2019) 104130.

Graphical Abstract

Here, an effective synergistic stabilization strategy using TBABr leads to *in situ* formation of 1D $TBAPbI_3$ capping layer and the Br-induced crystal secondary growth, which help effectively passivate the defects of $CsPbI_3$ perovskite for efficient and stable inorganic perovskite photovoltaics.

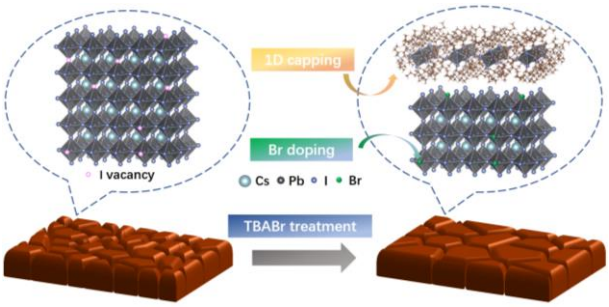

Supporting Information

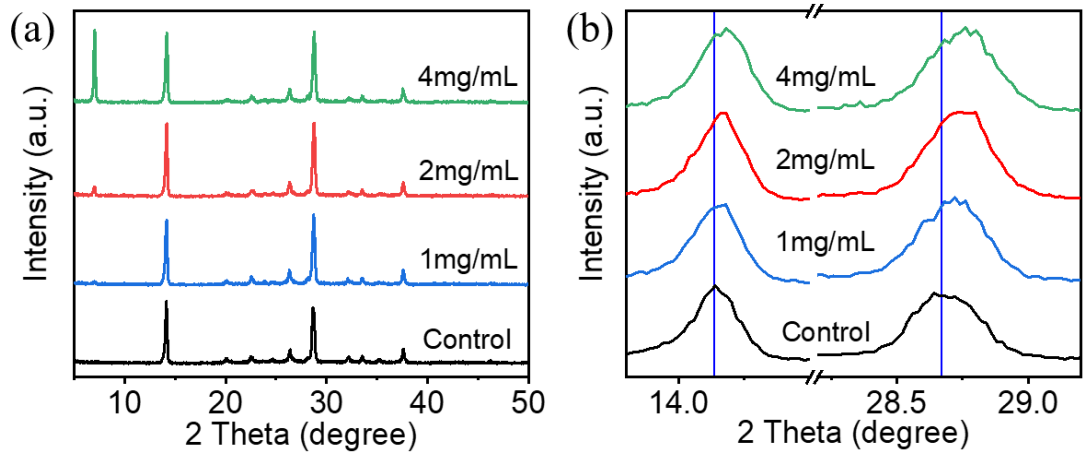

Fig. S1. (a) XRD patterns of the $CsPbI_3$ thin films treated with TBABr of different concentrations. (b) Magnified (110) and (220) diffraction peaks.

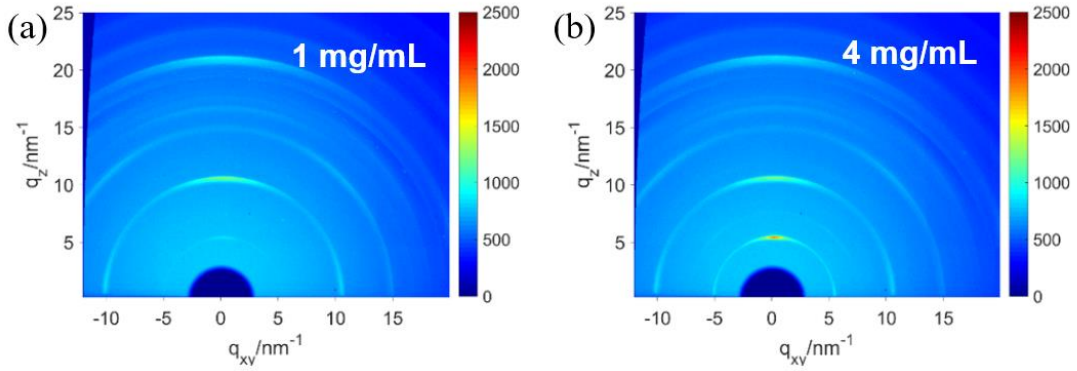

Fig. S2. GIWAXS data of the $CsPbI_3$ thin films treated with TBABr of different concentrations: (a) 1mg/mL and (b) 4mg/mL.

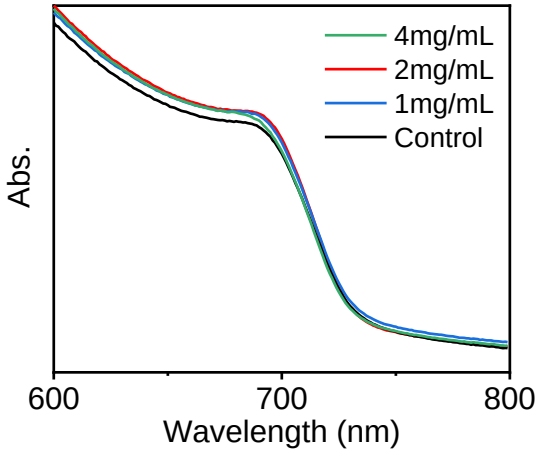

Fig. S3. UV-Vis spectra of the $CsPbI_3$ thin films treated by TBABr of different concentrations.

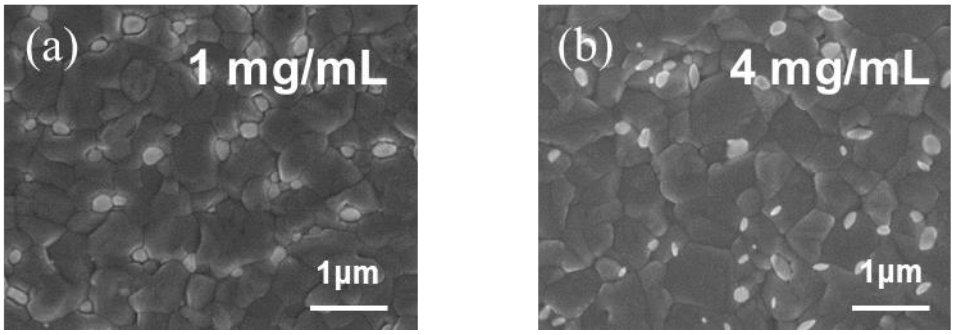

Fig. S4. SEM images of the $CsPbI_3$ thin films treated with different concentrations of (a) 1mg/mL and (b) 4mg/mL.

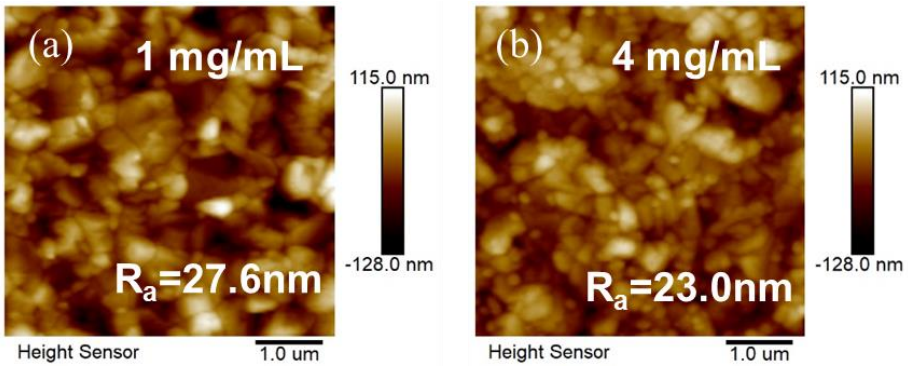

Fig. S5. AFM images of the $CsPbI_3$ thin films treated with different concentrations of (a) 1mg/mL and (b) 4mg/mL, respectively.

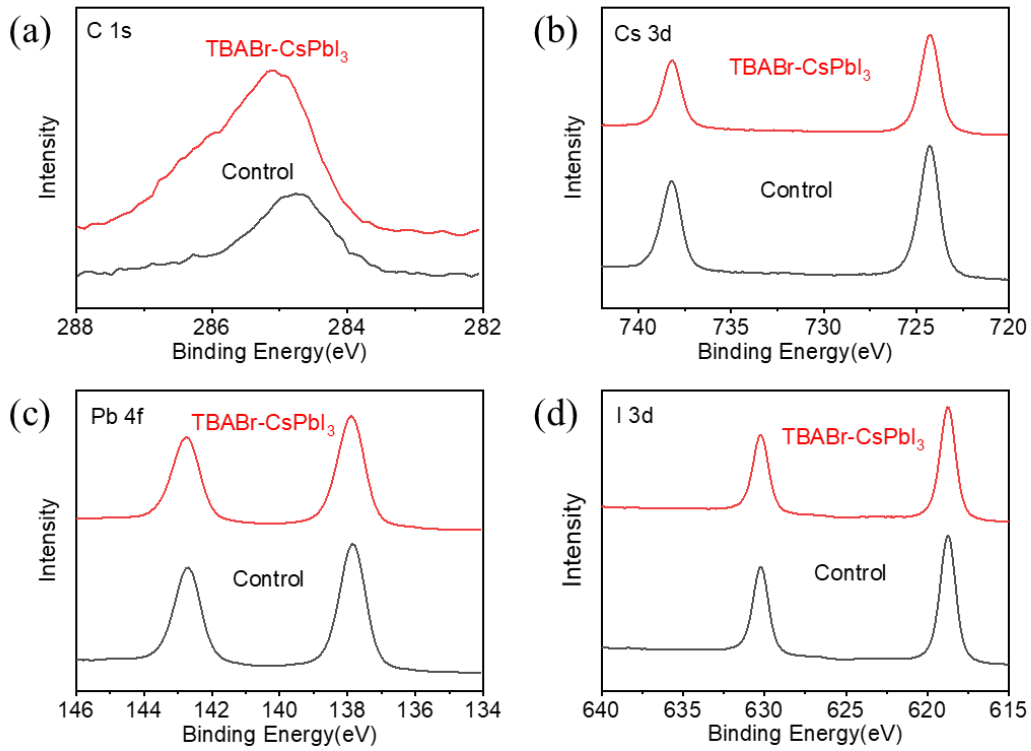

Fig. S6. High resolution XPS (a) C *1s*, (b) Cs *3d*, (c) Pb *4f*, and (d) I *3d* core-level spectra for the $CsPbI_3$ and TBABr-$CsPbI_3$ films.

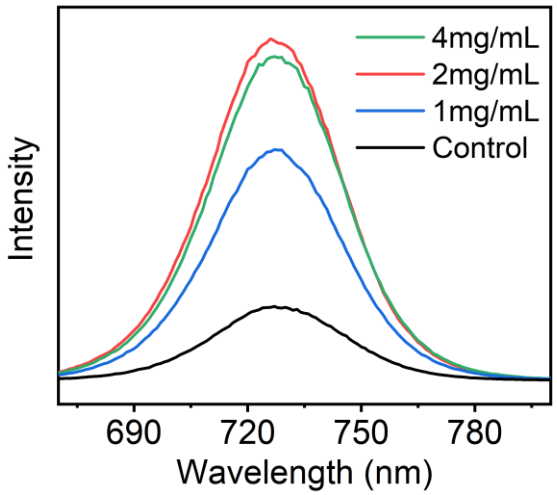

Fig. S7. PL spectra of the $CsPbI_3$ thin films treated by TBABr with different concentrations.

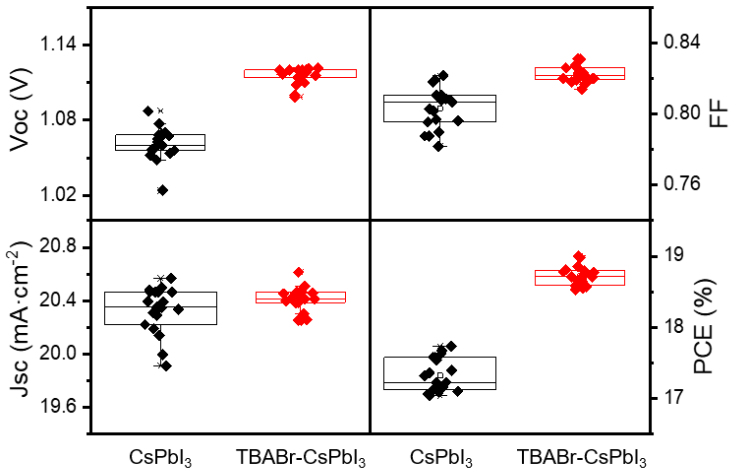

Fig. S8. Statistical box chart of photovoltaic parameters of the $CsPbI_3$ and TBABr-$CsPbI_3$ based PSCs.

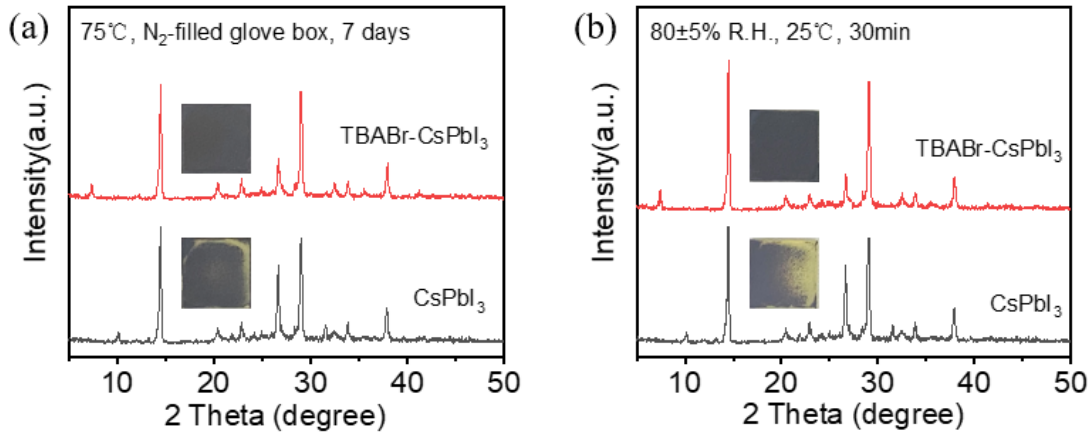

Fig. S9. XRD patterns and photos of different stability test results. (a) Thermal test: $CsPbI_3$ and TBABr-$CsPbI_3$ thin films heated at 75 °C in a N_2 glovebox for 7 days. (b) Humidity test: $CsPbI_3$ and TBABr-$CsPbI_3$ thin films after exposed to 80 ± 5% RH at ~25 °C for 30 min.

Table S1 Parameters of the $CsPbI_3$ and TBABr-$CsPbI_3$ thin films extracted from UPS characterization.

	E_{cutoff} (eV)	E_{onset} (eV)	E_c (eV)	E_v (eV)	WF (eV)	E_g (eV)
$CsPbI_3$	17.82	1.51	3.21	4.89	3.38	1.68
TBABr-$CsPbI_3$	17.41	1.50	3.60	5.29	3.79	1.69

Table S2 Charge carrier lifetimes within the $CsPbI_3$ and TBABr-$CsPbI_3$ thin films extracted from TRPL measurements.

	τ_{ave} (ns)	τ_1 (ns)	Amplitude of τ_1 (%)	τ_2 (ns)	Amplitude of τ_2 (%)
$CsPbI_3$	6.86	2.68	68.96	9.48	31.04
TBABr-$CsPbI_3$	28.37	12.94	47.36	33.70	52.64